

Quantum simulation of 2D antiferromagnets with hundreds of Rydberg atoms

<https://doi.org/10.1038/s41586-021-03585-1>

Received: 21 December 2020

Accepted: 27 April 2021

Published online: 7 July 2021

 Check for updates

Pascal Scholl^{1,6}✉, Michael Schuler^{2,6}, Hannah J. Williams^{1,6}, Alexander A. Eberharter^{3,6}, Daniel Barredo^{1,4}, Kai-Niklas Schymik¹, Vincent Lienhard¹, Louis-Paul Henry⁵, Thomas C. Lang³, Thierry Lahaye¹, Andreas M. L auchli³ & Antoine Browaeys¹

Quantum simulation using synthetic systems is a promising route to solve outstanding quantum many-body problems in regimes where other approaches, including numerical ones, fail¹. Many platforms are being developed towards this goal, in particular based on trapped ions^{2–4}, superconducting circuits^{5–7}, neutral atoms^{8–11} or molecules^{12,13}. All of these platforms face two key challenges: scaling up the ensemble size while retaining high-quality control over the parameters, and validating the outputs for these large systems. Here we use programmable arrays of individual atoms trapped in optical tweezers, with interactions controlled by laser excitation to Rydberg states¹¹, to implement an iconic many-body problem—the antiferromagnetic two-dimensional transverse-field Ising model. We push this platform to a regime with up to 196 atoms manipulated with high fidelity and probe the antiferromagnetic order by dynamically tuning the parameters of the Hamiltonian. We illustrate the versatility of our platform by exploring various system sizes on two qualitatively different geometries—square and triangular arrays. We obtain good agreement with numerical calculations up to a computationally feasible size (approximately 100 particles). This work demonstrates that our platform can be readily used to address open questions in many-body physics.

Previous studies have demonstrated the potential of Rydberg-based quantum simulators with up to a few tens of atoms^{14–16}, including high-fidelity manipulations^{17–19}. In particular, the transverse-field Ising (TFI) model has been studied in one dimension with up to 51 atoms^{14,15,20}, in two-dimensional (2D) square arrays—but with a limited degree of coherence^{16,21}, making it difficult to observe genuine quantum features—and recently in three dimensions with 22 atoms²². Here we implement the TFI model in two dimensions, combining much larger atom numbers (up to around 200) and a high degree of coherence. In our implementation, we explore two geometries that exhibit qualitatively different phase diagrams: the bipartite square lattice and the geometrically frustrated triangular lattice²³. On the square lattice, we prepare the N eel state that is characteristic of antiferromagnets with unprecedented probability. On the triangular lattice, we observe the creation of two distinct antiferromagnetic (AF) orders. The large number of atoms involved and the non-equilibrium nature of the experiment makes a direct comparison with accurate numerical simulations challenging. To validate the dynamics of our simulator, we have pushed matrix-product-state simulations to their limit and are able to simulate the dynamics of up to 100 atoms in two dimensions. We obtain an impressive agreement between the simulation and the experiment up to this number, which is one of the largest for which a direct comparison has been performed. Finally, by comparing the experiment to classical Monte Carlo calculations, we demonstrate that our results cannot be

reproduced by a classical equilibrium distribution at the same mean energy, and that the experiment features an enhanced probability of finding classical ground states.

2D quantum Ising model on a Rydberg simulator

For arrays of atoms coupled by the (repulsive) van der Waals interaction, when excited to Rydberg states, the Hamiltonian of the TFI model is:

$$H_{\text{Ryd}} = \sum_{i < j} U_{ij} n_i n_j + \frac{\hbar \Omega}{2} \sum_i \sigma_i^x - \hbar \delta \sum_i n_i, \quad (1)$$

where the Rydberg and ground states are mapped onto the (pseudo-) spin states $|\uparrow\rangle$ and $|\downarrow\rangle$, respectively. Here $U_{ij} = C_6/r_{ij}^6$ is the van der Waals interaction, C_6 is the van der Waals coefficient, r_{ij} is the distance between atoms i and j , $n_i = |\uparrow\rangle\langle\uparrow|_i = (1 + \sigma_i^z)/2$, σ_i are the usual Pauli matrices and \hbar is the reduced Planck's constant. The two spin states are coupled via a laser field with a Rabi frequency Ω and a detuning δ , which act as transverse and longitudinal fields, respectively. AF ordering in the system appears as a consequence of the strong interactions characterized by the Rydberg blockade radius R_b , as illustrated in Fig. 1a²⁴. The type of AF ordering depends on the geometry of the array and the Hamiltonian parameters.

¹Laboratoire Charles Fabry, Institut d'Optique Graduate School, Universit  Paris-Saclay, CNRS, Palaiseau, France. ²Vienna Center for Quantum Science and Technology, Atominstut, TU Wien, Vienna, Austria. ³Institut f r Theoretische Physik, Universit  Innsbruck, Innsbruck, Austria. ⁴Nanomaterials and Nanotechnology Research Center (CINN-CSIC), Universidad de Oviedo (UO), Principado de Asturias, El Entrego, Spain. ⁵Zentrum f r Optische Quantentechnologien, Institut f r Laser-Physik, Universit  Hamburg, Hamburg, Germany. ⁶These authors contributed equally: Pascal Scholl, Michael Schuler, Hannah J. Williams, Alexander A. Eberharter. ✉e-mail: pascal.scholl@institutoptique.fr

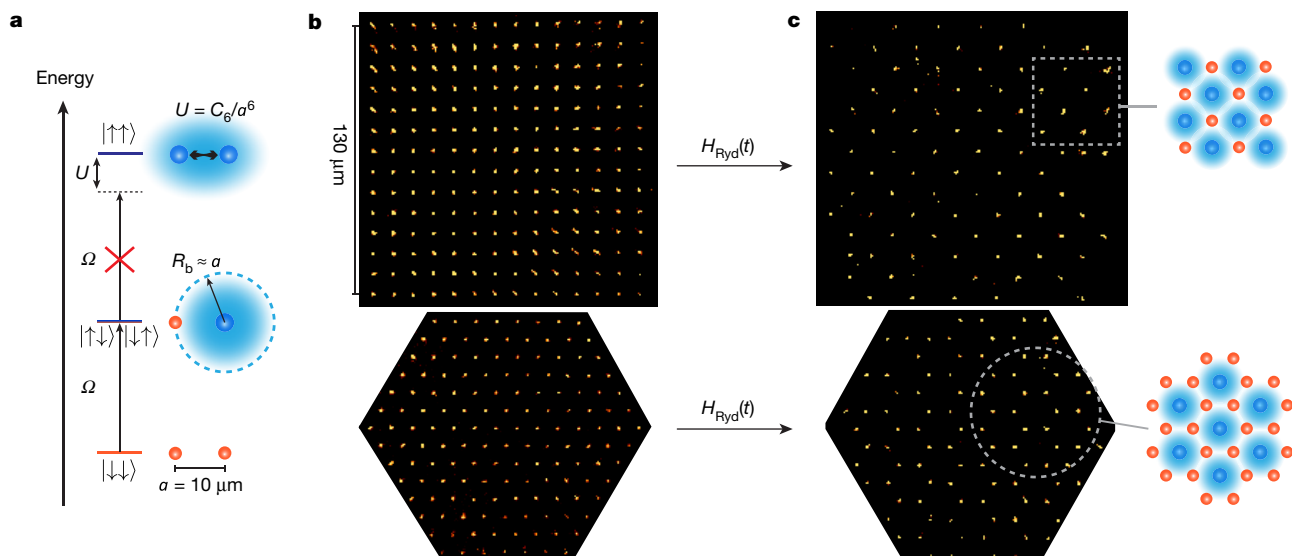


Fig. 1 | Emergence of AF ordering from the Rydberg blockade in square and triangular arrays. **a**, Illustration of the Rydberg blockade with two atoms, whereby the strong interactions prevent the simultaneous excitation of two atoms from the ground state (red circles) to the Rydberg state (blue circles)

within the Rydberg blockade radius R_b at which $U = \hbar\Omega$. **b, c**, Single-shot fluorescence images of ground state ($|\downarrow\rangle$) atoms in a 14×14 square array (top) and a 147-atom triangular array (bottom) with an atomic separation of $a = 10 \mu\text{m}$. **b**, Initial PM states. **c**, Nearly perfect AF ordering.

We create defect-free square and triangular arrays of up to 196 and 147^{87}Rb atoms, respectively, using an optimized atom-by-atom assembly protocol²⁵ (Fig. 1b). We define $|\downarrow\rangle = |5S_{1/2}, F=2, m_F=2\rangle$ and $|\uparrow\rangle = |7S_{1/2}, m_j=1/2\rangle$ (F and m_F are the hyperfine quantum numbers and m_j is the magnetic quantum number for the fine structure), which are coupled via the intermediate state $|6P_{3/2}, F=3, m_F=3\rangle$ with two counter-propagating laser beams with wavelengths of 420 nm and 1,013 nm (ref. ²⁶) (see ‘Experimental setup’ section). We achieve a single atom excitation probability of 99.1(8)% and a coherence time of 20 μs , about 20 times longer than in our previous work¹⁶ (see ‘Coherence of single-atom laser excitation’ section). We use arrays with atomic spacing $a = 10 \mu\text{m}$, leading to a nearest-neighbour interaction of $U/\hbar \approx 1.95 \text{ MHz}$.

To probe the phase diagram of H_{Ryd} , we sweep Ω and δ over time, and transfer the system from its initial paramagnetic (PM) ground state $|\downarrow \downarrow \dots \downarrow\rangle$ into the AF phase. A quantum phase transition (QPT) separates these two phases. Ideally, one would adiabatically drive the system such that it remains in the instantaneous ground state. However, the energy gap at the QPT decreases with the atom number N , (proportional to $1/\sqrt{N}$ on a square lattice and exponentially for the triangular lattice^{27,28}). This leads to timescales that are experimentally impractical due to decoherence effects, dominated by spontaneous emission from the intermediate state. Hence, we choose sweep times (about 6 μs) that are short enough to avoid sizeable decoherence but sufficiently long to quasi-adiabatically probe the phase diagram (see ‘Benchmarking the 4×4 array’ section). We record fluorescence images of the atoms remaining in $|\downarrow\rangle$. Examples of single-shot images of the largest square and triangular arrays before (and following) the preparation sweeps are shown in Fig. 1b, c. The final images show almost-perfect AF ordering. For the results presented here, we typically repeat the sequence 1,000 times.

Antiferromagnet on the square lattice

We first focus on the square lattice, using arrays of size $N = L \times L$, with an even linear system size L so that the two Néel states have the same energy. In Fig. 2a, we sketch the (bulk) phase diagram. In the case of the van der Waals interaction implemented here, the AF phase region is expected to extend up to the critical point $\hbar\Omega_c \approx 1.25U$ at $\hbar\delta \approx 4.66U/2$

(ref. ²⁹). More complex phases³⁰, explored in a companion paper³¹, appear at the lower and upper boundaries of $\hbar\delta/U$ in the AF region. The applied sweeps are shown in Fig. 2a, with the QPT being crossed during the ramp down of $\Omega(t)$. Figure 2b presents an experimental histogram of the states recorded at the end of the sweep for the 8×8 array. Remarkably, out of $2^{64} \approx 2 \times 10^{19}$ possible states, we obtain a perfectly ordered state with a probability of around 2.5% (including detection errors; even if the sweeps were fully adiabatic, the probability of measuring perfect AF ordering would be about 27% due to our detection errors), as can be seen by the two prominent peaks. The fluorescence images show the two corresponding Néel states. To characterize the magnetic ordering of the states prepared during the sweep, we measure the order parameter, which is the normalized staggered magnetization $m_{\text{stag}} = \langle |n_A - n_B| \rangle / (N/2)$, giving the difference in the number of excitations on each sublattice (A and B), averaged over many realizations. The two perfect AF states correspond to one of the two sublattices being fully excited, such that $m_{\text{stag}} = 1$. We access the dynamics of the system during the sweep by rapidly turning off the excitation laser at different times t_{off} (Fig. 2a). Figure 2c shows the evolution of m_{stag} for the 6×6 array and the 10×10 array, using the same sweep. Over the first 1.5 μs of the sweep, the system is in the PM phase, where fluctuations lead to small but finite $m_{\text{stag}} \propto 1/\sqrt{N}$. We then observe the growth of m_{stag} during the drive of the system from the PM to the AF phase.

To benchmark our platform, we perform a systematic comparison of the dynamics with matrix product state (MPS) numerical simulations (see ‘Matrix product states’ section). We consider both the programmed and the real parameters, the latter of which include independently calibrated experimental imperfections (detection errors, inhomogeneities of the excitation beams, pulse shapes and residual disorder in the atomic positions, described in detail in the ‘Effect of imperfections on larger arrays’ section), with the exception of decoherence effects. For the 6×6 array, we observe a good agreement between the experimental results and the MPS simulations, for both situations. For the 10×10 array, the experiment and the real MPS simulations also agree well. The difference between the programmed and the real MPS simulations highlights that the imperfections have a more severe impact on larger systems. In addition, the reduced final value of m_{stag} for the programmed MPS on the 10×10 array indicates that as the system size grows, adiabaticity is indeed harder to achieve.

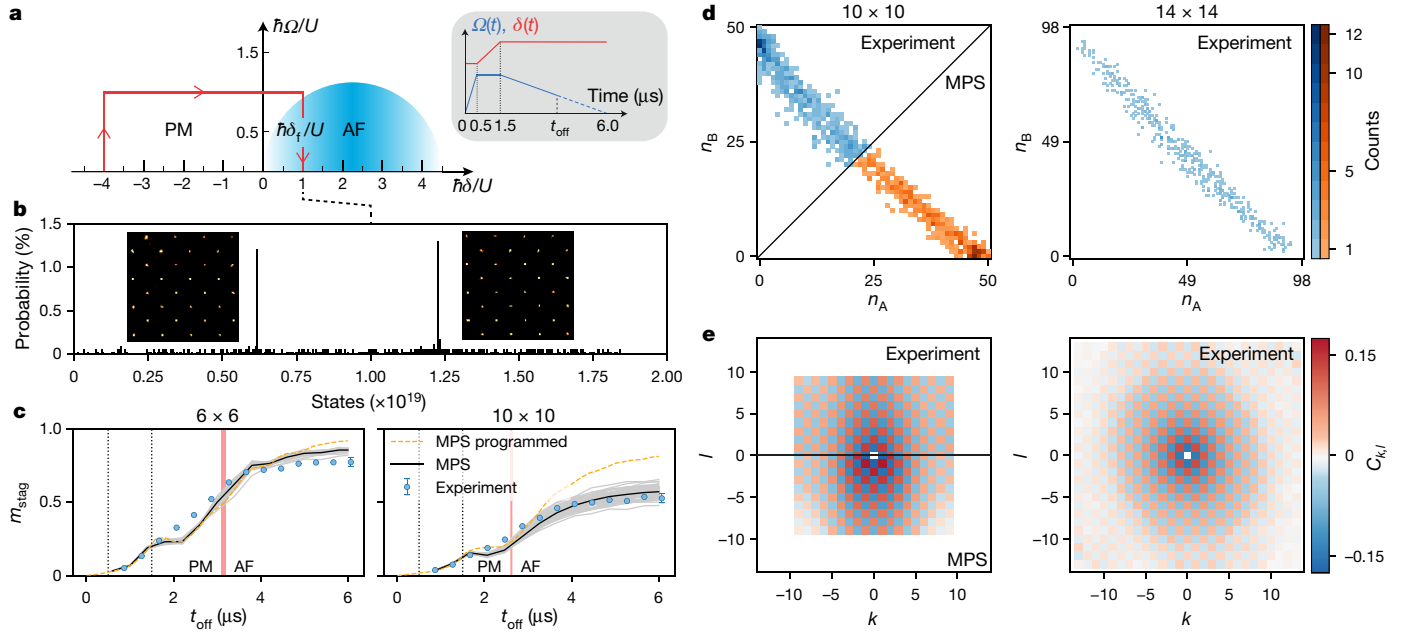


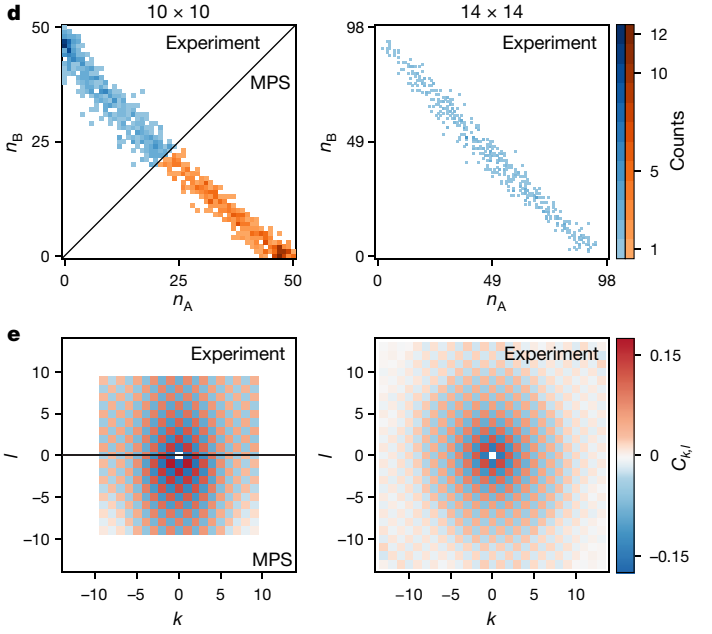
Fig. 2 | The Ising model on a square lattice. **a**, Sketched bulk phase diagram for the square lattice. The inset shows the sweep shape, with t_{off} the switch-off time of the excitation laser. The corresponding trajectory in the phase diagram is shown as a red arrow. **b**, State histogram for the 8×8 array at the end of the sweep. The insets show fluorescence images of the two perfect AF states, which are obtained with 2.5% probability. **c**, Growth of the staggered magnetization during the sweep for the 6×6 array (left) and the 10×10 array (right). The blue circles are experimental results with standard errors on the mean smaller than the markers size. The error bar on the final point is indicative of the long-term stability of the experimental setup (see ‘Long-term stability’ section). MPS

We now characterize the final state obtained at the end of the sweep ($\Omega = 0$). First, we visualize the shot-wise contributions to m_{stag} using a 2D histogram of the probability $P(n_A, n_B)$ of the $|\uparrow\rangle$ populations n_A and n_B of the two sublattices A and B. Here the two Néel states appear as points at $(N/2, 0)$ and $(0, N/2)$. The results are plotted in Fig. 2d for the 10×10 array and the 14×14 array. For both systems, we observe the presence of points along the diagonal, highlighting that the average Rydberg density is about 50%. For the 10×10 array, we observe a conglomeration of points around the two corners belonging to the Néel states. Owing to the imperfections and the scaling of the energy gap, the state preparation becomes more challenging with increasing system size. The elongated histogram for the 14×14 array demonstrates that, remarkably, we prepare strongly AF ordered states ($m_{\text{stag}} = 0.391(1)$), even for such large systems. This is also evident in the fluorescence image in Fig. 1c, which shows 184 atoms (out of 196) obeying AF ordering. For a comparison with simulations, we have devised an algorithm to stochastically sample the MPS wavefunction, thereby obtaining snapshots as in the experiment (see ‘Sampling of MPS wavefunctions’ section). The lower half of Fig. 2d shows the so-obtained histogram for the 10×10 lattice, which matches the experiment very well. For even larger atom numbers, accurate MPS simulations become intractable.

Second, we compute the connected spin–spin correlation function defined as

$$C_{k,l} = \frac{1}{N_{k,l}} \sum_{i,j} \langle n_i n_j \rangle - \langle n_i \rangle \langle n_j \rangle, \quad (2)$$

where the sum runs over all pairs of atoms i and j separated by $k\mathbf{e}_1 + l\mathbf{e}_2$, with $\mathbf{e}_{1(2)}$ denoting the two vectors of the underlying lattice, k and l are two integer numbers, and $N_{k,l}$ being the number of such pairs. Figure 2e shows the $C_{k,l}$ correlation maps corresponding to the m_{stag} histograms



simulations without (dashed line) and with (grey lines) experimental imperfections for which 50 (6×6 array) and 77 (10×10 array) disorder instances are shown, with their average shown in black. The vertical dotted lines correspond to the turning points in the sweep. The vertical red regions depict the finite-size phase boundaries between the PM and AF phases, obtained from the inflection point of m_{stag} using ground state density matrix renormalization group. **d**, Final staggered magnetization histograms for the 10×10 array (left) and the 14×14 array (right). **e**, The correlation maps for the 10×10 array (left) and the 14×14 array (right), with the MPS results shown in the lower half for the 10×10 array.

shown in Fig. 2d. The plots show the alternation of correlation and anti-correlation, expected for AF ordering, whose values would be $\pm 1/4$ for the Néel state. The spatial decay of the correlations is well described by correlation lengths of $\xi \approx 7a$ and $\xi \approx 5.5a$ for the two system sizes, respectively, showing that the sweeps produce highly AF ordered states (the residual anisotropy observed is due to the finite size of the excitation beams, which is comparable to the width of the array ($130 \mu\text{m}$)). Again, we observe good agreement between the experimental and real MPS results for the 10×10 array, confirming that the simulations capture well the experimental conditions (for a real-time analysis of the correlations during the sweep, see the ‘Growth of antiferromagnetic order’ section).

Comparison with classical thermal equilibrium

To further quantify the AF ordering, we analyse the distribution of AF cluster sizes³². For each run of the experiment, we decompose the snapshot into individual clusters obeying local AF ordering (see examples in Fig. 3a, b). We count the number of atoms inside each individual cluster, and record the largest size, s_{max} . From the full set of snapshots, we reconstruct the probability distribution $P(s_{\text{max}})$. For a perfectly AF-ordered state, this distribution presents as a single peak of unit probability at $s_{\text{max}} = N$, while imperfect ordering shows up as a distribution broadened towards smaller s_{max} . In Fig. 3c, d we show $P(s_{\text{max}})$ at the end of the sweep for the 10×10 array obtained from the experiment (Fig. 3c) and from MPS simulations (Fig. 3d). We observe that more than 27% (30%) of the shots in the experiment (MPS) contain AF clusters of at least 90 sites, that is, $s_{\text{max}} \geq 90$.

The fact that we obtain a distribution of final states raises the question whether the system has thermalized during the finite duration of the sweep^{14,33}. To answer this question, we compare the observed distribution $P(s_{\text{max}})$ to the corresponding distribution obtained from a classical

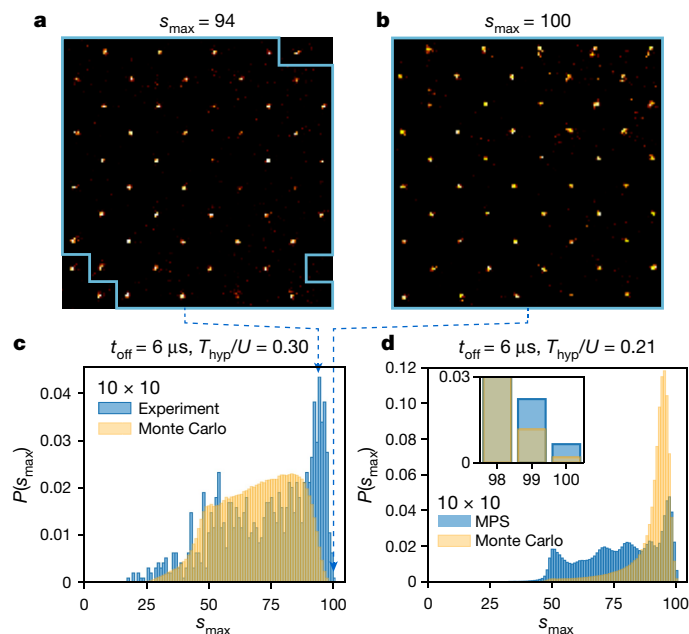


Fig. 3 | Quantum real-time evolution versus classical equilibrium. **a, b**, Fluorescence images on a 10×10 array illustrating how we extract the largest AF domains comprising 94 (**a**) and 100 (**b**) sites, indicated by the blue boundaries. **c, d**, Distributions of s_{\max} at the end of the sweep (blue) compared with the classical equilibrium result (yellow) with the corresponding hypothetical temperature T_{hyp} , obtained from the experiment (**c**) and MPS simulations (**d**). The inset in **d** is a zoom into the distribution of the largest AF domains.

equilibrium setup with a hypothetical temperature T_{hyp} . We focus on a classical description for two reasons: (1) the classical energy is the one accessible in the experiment and (2) at the end of the sweep, $\Omega = 0$ and the quantum and classical statistical mechanics descriptions coincide.

To determine T_{hyp} , we match the classical Ising energy $E_{\text{class}}(t_{\text{off}})$ of the experimental system with $E_{\text{class}}^{\text{MC}}(T)$ from the corresponding classical statistical mechanics system for a given temperature T estimated from a Monte Carlo sampling (one could also use other observables to match a hypothetical temperature, but as temperature is the variable conjugate to the energy in thermodynamics, it is the most natural choice). We refer to the ‘Extracting a classical temperature’ section for a thorough discussion of T_{hyp} during the sweep. In Fig. 3c, d, we show $P(s_{\max})$ for the corresponding classical equilibrium distributions, and observe that they do not reproduce the distribution of the experimental and MPS results. In particular, the probability of creating perfectly ordered states is higher in the quantum real-time evolution than in the classical equilibrium case. The classical equilibrium approach also results in shorter correlation lengths. A similar analysis during the sweep and for the MPS real-time evolution shows similar features (see the ‘Experiment versus classical equilibrium during the sweep’ and ‘MPS time evolution versus classical equilibrium’ sections). Our analysis therefore reveals that despite residual imperfections, the experiment does not thermalize during the state preparation protocol and is well reproduced by a unitary quantum mechanical real-time description. Furthermore, the enhanced probability of finding the targeted classical states is promising for future applications of the Rydberg platform, for example, as a quantum annealer to solve optimization problems of various types^{34–36}.

The 1/3 and 2/3 phases on the triangular lattice

Having explored the square lattice, we now consider the more complex triangular array. Here the TFI model features a richer phase diagram,

with prominent ordered phases at 1/3 and 2/3 Rydberg filling, as sketched in Fig. 4a. The 1/3 phase is the analogue of the AF ordering on the square lattice, where the Rydberg blockade prevents neighbouring sites from being excited simultaneously, leading to one of the three sublattices being filled with Rydberg excitations, illustrated in Fig. 1c. The 2/3 phase is the ‘particle–hole’ inverse of this, with two sublattices being fully excited and one sublattice containing ground-state atoms. In between these phase regions, at 1/2 filling, the classical Ising model ($\Omega = 0$) is strongly frustrated for nearest-neighbour interactions, with an exponentially large (in N) ground-state manifold²³. Finite Ω stabilizes yet another ordered phase in a process called ‘order by disorder’ (OBD)^{29,37–41}.

To explore the triangular phase diagram, we consider hexagonal clusters of various sizes, built shell by shell around a central three-atom triangle (Fig. 1b). We apply the sweeps shown in Fig. 4a for two different final detunings, δ_f , to create the 1/3 and the 2/3 phases. To quantify the state preparation process, we again measure the temporal dynamics of the order parameter, the normalized staggered magnetization. For the triangular array, this is defined as $m_{\text{stag}} = \langle |n_A + e^{i2\pi/3}n_B + e^{-i2\pi/3}n_C| \rangle / (N/3)$, where $n_{A,B,C}$ is the Rydberg population on each of the three sublattices. We plot the results in Fig. 4b for the experiment and two types of MPS simulation (programmed and real) for a 75-atom array, with δ_f chosen to prepare the 1/3 phase. We observe the growth of the AF ordering both in the experiment and the simulations, which agree well during the first 5 μs of the sweep. After this, the experimental results plateau at a lower value of m_{stag} than expected from the MPS. The inclusion of experimental imperfections decreases the final value of m_{stag} ; however, there is still a discrepancy with the experimental results. A possible explanation could be the enhanced sensitivity of the QPT from PM to the 1/3 AF phase (believed to be first order²⁷) to the residual experimental imperfections not included in the MPS simulation. Confirming the origin of this effect will be the subject of future work.

To further characterize the prepared final states, we consider $C_{k,l}$, defined similarly to equation (2). Here the perfect AF state would have $C_{k,l} = +2/9$ and $C_{k,l} = -1/9$ for correlated and anticorrelated sites, respectively. In Fig. 4c, e, we show the final-state correlation maps for the 1/3 (2/3) phases on atom arrays of 75, 108 and 147 sites (108 sites). We observe a pattern characteristic of three-sublattice ordered states, throughout almost the entire bulk of our systems, with a correlation length $\xi \approx 3-3.7a$ for the 1/3 phase and $\xi \approx 2a$ for the 2/3 phase. In Fig. 4d, f, we plot the corresponding distributions of the complex order parameter. For perfectly ordered 1/3 (2/3) systems, one would expect peaks at the three corners of the bounding hexagon, marked by red (green) dots. We observe correspondingly aligned triangular distributions with good agreement between the experimental and MPS results. There is a higher accumulation of points at the corners in the MPS results, which corresponds to a higher value of m_{stag} . Although the distributions spread almost fully to the corners in the 1/3 phase results, for the 2/3 phase the size of the triangle is visibly reduced. This reduction is due to finite-size cluster effects: the boundary is filled with Rydberg excitations, which reduces the maximal possible extent of the distribution to the inner hexagon (dashed lines) (see ‘Triangular 2/3 plateau’ section). The above results demonstrate the preparation of the 1/3 and 2/3 phases using a synthetic quantum many-body system. Despite the experimental imperfections, and the finite sweep duration, we are able to produce highly ordered states on even the largest 147-atom array. This is highlighted in Fig. 1c, which shows a fluorescence image of the 1/3 phase on the 147-atom array with almost perfect AF ordering. Finally, similar to the square array, we observe an enhanced probability of finding highly ordered states compared with a classical equilibrium system at the same energy, as revealed by experimental order parameter distributions that are centred at larger values (see details in the ‘Time evolution versus classical equilibrium on the triangular lattice’ section).

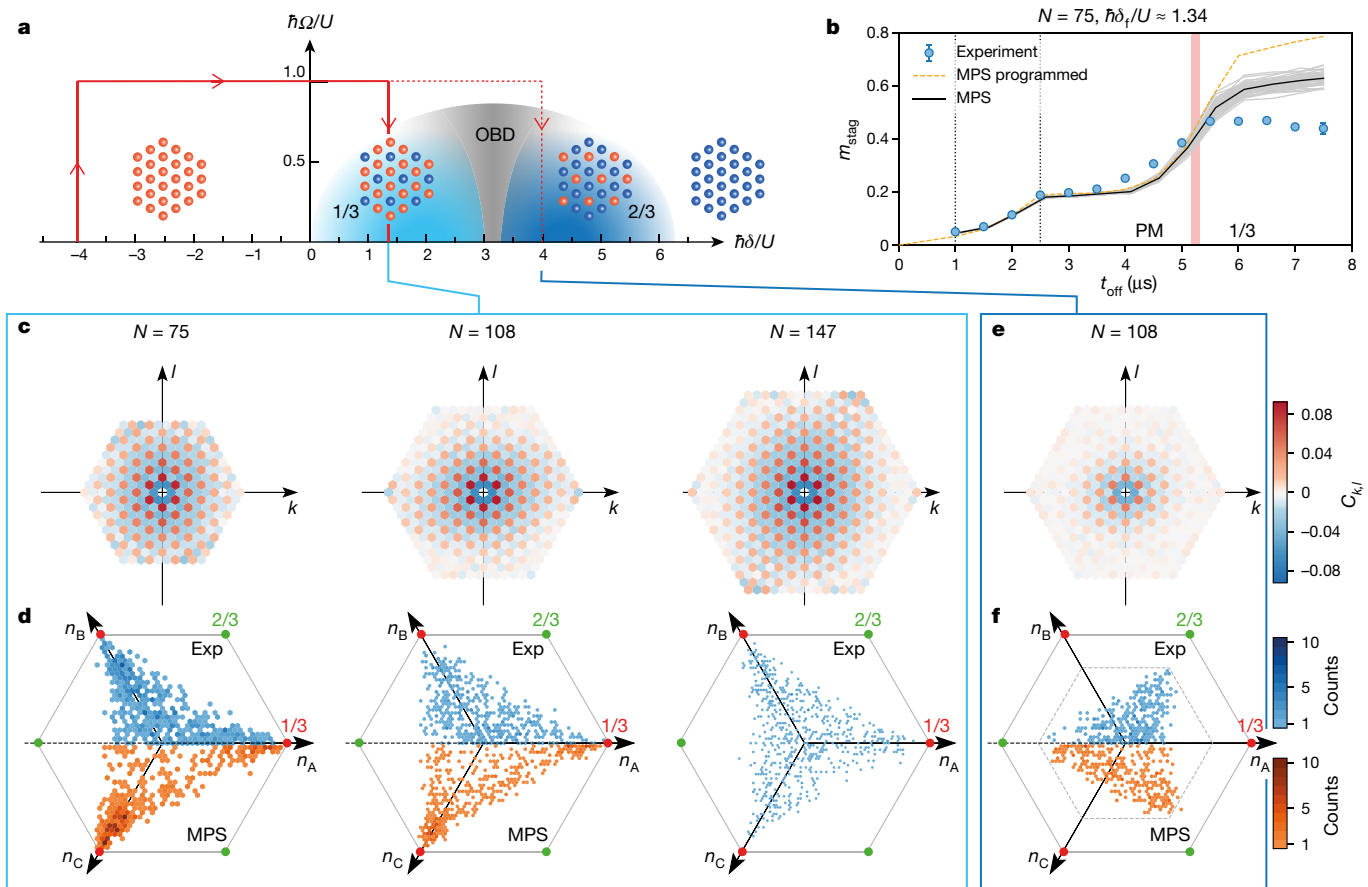


Fig. 4 | AF ordering on a triangular array. **a**, Sketched bulk phase diagram for the triangular lattice. The red arrows show the sweeps used to prepare the phases at 1/3 and 2/3 filling. **b**, Growth of the staggered magnetization during the sweep for a 75-atom array. The blue circles are experimental results with standard errors on the mean smaller than the markers size. The error bar on the final point is indicative of the long-term stability of the experimental setup (see ‘Long-term stability’ section). MPS simulations without (dashed line) and with (grey lines) experimental imperfections for which 50 disorder instances are shown, with their average shown in black. The vertical dotted lines correspond to the turning points in the sweep. The vertical red region depicts the finite-size

phase boundary between the PM and the 1/3 AF phase phases obtained from density matrix renormalization group. **c, d**, Final experimental correlation maps (**c**) and corresponding staggered magnetization histograms plotted in the complex plane (**d**) for the 75-site (left), 108-site (middle) and 147-site (right) triangular arrays for the sweep preparing the 1/3 phase. For the 75-site and 108-site arrays, the lower half of the histograms show the analogous MPS results. **e, f**, Final experimental correlation map (**e**) and corresponding staggered magnetization histogram (**f**) for the 108-site triangular array for the sweep preparing the 2/3 phase. The lower half of **f** shows the corresponding MPS results.

Conclusions and outlook

We have probed the quantum dynamics of Ising magnets in square and triangular geometries, beyond situations that can be exactly simulated classically. We have validated the experimental results with comprehensive numerical simulations up to computationally feasible sizes. We have shown a high degree of coherence and control, over a large number of atoms. Combined, this demonstrates that our platform is now able to study quantum spin models in regimes beyond those accessible via numerical investigations. We have also identified a potential advantage of Rydberg quantum simulators to prepare targeted classical states, compared with classical equilibrium systems. Natural extensions of this work include a thorough investigation of the dynamics of the 2D QPT, and further explorations of the effects of frustration, in particular the observation of the elusive OBD phase. Finally, our benchmark provides a roadmap for improving the platform even further, thus opening exciting prospects beyond quantum simulation, for example, for optimization^{34,36}, quantum sensing^{42,43} and quantum computing^{44–46}.

Independent work exploring other phases and dynamics on a square array with a Rydberg quantum simulator is reported in a companion publication³¹.

Online content

Any methods, additional references, Nature Research reporting summaries, source data, extended data, supplementary information, acknowledgements, peer review information; details of author contributions and competing interests; and statements of data and code availability are available at <https://doi.org/10.1038/s41586-021-03585-1>.

- Georgescu, I. M., Ashhab, S. & Nori, F. Quantum simulation. *Rev. Mod. Phys.* **86**, 153–185 (2014).
- Blatt, R. & Roos, C. F. Quantum simulations with trapped ions. *Nat. Phys.* **8**, 277–284 (2012).
- Monroe, C. et al. Programmable quantum simulations of spin systems with trapped ions. *Rev. Mod. Phys.* **93**, 025001 (2021).
- Gärtner, M. et al. Measuring out-of-time-order correlations and multiple quantum spectra in a trapped-ion quantum magnet. *Nat. Phys.* **13**, 781–786 (2017).
- Song, C. et al. 10-qubit entanglement and parallel logic operations with a superconducting circuit. *Phys. Rev. Lett.* **119**, 180511 (2017).
- King, A. D. et al. Observation of topological phenomena in a programmable lattice of 1,800 qubits. *Nature* **560**, 456–460 (2018).
- Kjaergaard, M. et al. Superconducting qubits: current state of play. *Annu. Rev. Condens. Matter Phys.* **11**, 369–395 (2020).
- Bloch, I., Dalibard, J. & Zwirger, W. Many-body physics with ultracold gases. *Rev. Mod. Phys.* **80**, 885–964 (2008).
- Bloch, I., Dalibard, J. & Nascimbène, S. Quantum simulations with ultracold quantum gases. *Nat. Phys.* **8**, 267–276 (2012).

10. Gross, C. & Bloch, I. Quantum simulations with ultracold atoms in optical lattices. *Science* **357**, 995–1001 (2017).
11. Browaeys, A. & Lahaye, T. Many-body physics with individually controlled Rydberg atoms. *Nat. Phys.* **16**, 132–142 (2020).
12. Yan, B. et al. Observation of dipolar spin-exchange interactions with lattice-confined polar molecules. *Nature* **501**, 521–525 (2013).
13. Zhou, Y. L., Ortner, M. & Rabl, P. Long-range and frustrated spin–spin interactions in crystals of cold polar molecules. *Phys. Rev. A* **84**, 052332 (2011).
14. Bernien, H. et al. Probing many-body dynamics on a 51-atom quantum simulator. *Nature* **551**, 579–584 (2017).
15. Keesling, A. et al. Quantum Kibble–Zurek mechanism and critical dynamics on a programmable Rydberg simulator. *Nature* **568**, 207–211 (2019).
16. Lienhard, V. et al. Observing the space- and time-dependent growth of correlations in dynamically tuned synthetic Ising antiferromagnets. *Phys. Rev. X* **8**, 021070 (2018).
17. Levine, H. et al. Parallel implementation of high-fidelity multiqubit gates with neutral atoms. *Phys. Rev. Lett.* **123**, 170503 (2019).
18. Omran, A. et al. Generation and manipulation of Schrödinger cat states in Rydberg atom arrays. *Science* **365**, 570–574 (2019).
19. Madjarov, I. S. et al. High-fidelity entanglement and detection of alkaline-earth Rydberg atoms. *Nat. Phys.* **16**, 857–861 (2020); correction **17**, 144 (2021).
20. Schauß, P. et al. Crystallization in Ising quantum magnets. *Science* **347**, 1455–1458 (2015).
21. Guardado-Sanchez, E. et al. Probing the quench dynamics of antiferromagnetic correlations in a 2D quantum Ising spin system. *Phys. Rev. X* **8**, 021069 (2018).
22. Song, Y., Kim, M., Hwang, H., Lee, W. & Ahn, J. Quantum simulation of Cayley-tree Ising Hamiltonians with three-dimensional Rydberg atoms. *Phys. Rev. Res.* **3**, 013286 (2021).
23. Wannier, G. H. Antiferromagnetism. The triangular Ising net. *Phys. Rev.* **79**, 357–364 (1950).
24. Jaksch, D. et al. Fast quantum gates for neutral atoms. *Phys. Rev. Lett.* **85**, 2208–2211 (2000).
25. Schymik, K.-N. et al. Enhanced atom-by-atom assembly of arbitrary tweezer arrays. *Phys. Rev. A* **102**, 063107 (2020).
26. Levine, H. et al. High-fidelity control and entanglement of Rydberg-atom qubits. *Phys. Rev. Lett.* **121**, 123603 (2018).
27. Janke, W. & Villanova, R. Three-dimensional 3-state Potts model revisited with new techniques. *Nucl. Phys. B* **489**, 679–696 (1997).
28. Laumann, C. R., Moessner, R., Scardicchio, A. & Sondhi, S. L. Quantum adiabatic algorithm and scaling of gaps at first-order quantum phase transitions. *Phys. Rev. Lett.* **109**, 030502 (2012).
29. Fey, S., Kapfer, S. C. & Schmidt, K. P. Quantum criticality of two-dimensional quantum magnets with long-range interactions. *Phys. Rev. Lett.* **122**, 017203 (2019).
30. Samajdar, R., Ho, W. W., Pichler, H., Lukin, M. D. & Sachdev, S. Complex density wave orders and quantum phase transitions in a model of square-lattice Rydberg atom arrays. *Phys. Rev. Lett.* **124**, 103601 (2020).
31. Ebadi, S. et al. Quantum phases of matter on a 256-atom programmable quantum simulator. *Nature* <https://doi.org/10.1038/s41586-021-03582-4> (2021).
32. Stoli, E. & Domb, C. Shape and size of two-dimensional percolation clusters with and without correlations. *J. Phys. A* **12**, 1843–1855 (1979).
33. Kim, H., Park, Y., Kim, K., Sim, H.-S. & Ahn, J. Detailed balance of thermalization dynamics in Rydberg-atom quantum simulators. *Phys. Rev. Lett.* **120**, 180502 (2018).
34. Pichler, H., Wang, S.-T., Zhou, L., Choi, S. & Lukin, M. D. Quantum optimization for maximum independent set using Rydberg atom arrays. Preprint at <https://arxiv.org/abs/1808.10816> (2018).
35. Henriët, L. Robustness to spontaneous emission of a variational quantum algorithm. *Phys. Rev. A* **101**, 012335 (2020).
36. Serret, M. F., Marchand, B. & Ayrál, T. Solving optimization problems with Rydberg analog quantum computers: realistic requirements for quantum advantage using noisy simulation and classical benchmarks. *Phys. Rev. A* **102**, 052617 (2020).
37. Villain, J., Bidaux, R., Carton, J.-P. & Conte, R. Order as an effect of disorder. *J. Phys. France* **41**, 1263–1272 (1980).
38. Moessner, R., Sondhi, S. L. & Chandra, P. Two-dimensional periodic frustrated Ising models in a transverse field. *Phys. Rev. Lett.* **84**, 4457–4460 (2000).
39. Moessner, R. & Sondhi, S. L. Ising models of quantum frustration. *Phys. Rev. B* **63**, 224401 (2001).
40. Isakov, S. V. & Moessner, R. Interplay of quantum and thermal fluctuations in a frustrated magnet. *Phys. Rev. B* **68**, 104409 (2003).
41. Koziol, J., Fey, S., Kapfer, S. C. & Schmidt, K. P. Quantum criticality of the transverse-field Ising model with long-range interactions on triangular-lattice cylinders. *Phys. Rev. B* **100**, 144411 (2019).
42. Madjarov, I. S. et al. An atomic-array optical clock with single-atom readout. *Phys. Rev. X* **9**, 041052 (2019).
43. Norcia, M. A. et al. Seconds-scale coherence on an optical clock transition in a tweezer array. *Science* **366**, 93–97 (2019).
44. Saffman, M., Walker, T. G. & Mølmer, K. Quantum information with Rydberg atoms. *Rev. Mod. Phys.* **82**, 2313–2363 (2010).
45. Henriët, L. et al. Quantum computing with neutral atoms. *Quantum* **4**, 327 (2020).
46. Morgado, M. & Whitlock, S. Quantum simulation and computing with Rydberg qubits. *AVS Quantum Sci.* **3**, 023501 (2021).

Publisher's note Springer Nature remains neutral with regard to jurisdictional claims in published maps and institutional affiliations.

© The Author(s), under exclusive licence to Springer Nature Limited 2021

Methods

Experimental setup

Our experimental setup, described in detail in ref. ⁴⁷, is based on arrays of single atoms trapped in optical tweezers. To create defect-free arrays consisting of N atoms, we begin with a stochastically loaded array containing $>2N$ traps and then, using a single, moving optical tweezer trap, rearrange the atoms into the desired configuration. Optimization of the rearrangement algorithms and the introduction of multiple cycles²⁵ have enabled us to create arbitrary arrays with up to 200 atoms: for example, the amount of time needed to assemble the 14×14 array went from about 350 ms to about 180 ms.

Following the rearrangement, the atoms are optically pumped into the ground state $|\downarrow\rangle = |5S_{1/2}, F=2, m_F=2\rangle$ in the presence of a static magnetic field of 7 G with 99.9% efficiency. The tweezers are then switched off for the duration of the sweeps. We use the Rydberg state $|\uparrow\rangle = |7S_{1/2}, m_J=1/2\rangle$ with a lifetime $\tau=175 \mu\text{s}$, and van der Waals coefficient $C_6/\hbar=1,947 \text{ GHz } \mu\text{m}^6$. To excite the atoms from $|\downarrow\rangle$ to $|\uparrow\rangle$, we drive a two-photon transition using counter-propagating laser beams with wavelengths of 420 nm and 1,013 nm, via the intermediate state $|6P_{3/2}, F=3, m_F=3\rangle$ with a lifetime of 113 ns. We use two titanium:sapphire lasers (M-Squared), because of their intrinsic low phase noise at high frequency⁴⁸. One, operating at 840 nm, is frequency doubled to 420 nm with up to 2 W, and the second, at 1,013 nm, seeds an AzurLight Systems fibre amplifier delivering up to 10 W. The 420-nm light is fibre coupled to the experiment, whereas the 1,013-nm light is free space. The $1/e^2$ radii and maximum powers of the lasers at the position of the atoms are $w_{420}=250 \mu\text{m}$, $P_{420}=350 \text{ mW}$, and $w_{1,013}=130 \mu\text{m}$, $P_{1,013}=5 \text{ W}$, allowing for Rabi frequencies of up to $\Omega_{420}=2\pi \times 200 \text{ MHz}$ and $\Omega_{1,013}=2\pi \times 50 \text{ MHz}$. To limit the spontaneous emission, the lasers are detuned by $2\pi \times 700 \text{ MHz}$ from the intermediate state, resulting in a maximum effective Rabi frequency of $\Omega=2\pi \times 7 \text{ MHz}$.

To detect the state of the atoms, the tweezers are turned back on, recapturing atoms in $|\downarrow\rangle$, which we then image. The atoms in $|\uparrow\rangle$ are repelled from the tweezers and hence are not imaged. This detection method features imperfections, described in detail in ref. ⁴⁸, which result in two types of error. First a false positive, with probability ε , where a ground-state atom is lost and misidentified as a Rydberg atom, and second a false negative, with probability ε' , where a Rydberg atom decays quickly, is recaptured and hence, misidentified as a ground-state atom. The results presented in the main text have $\varepsilon=1.0(2)\%$ and $\varepsilon'=3.0(1)\%$.

Matrix product states

To verify the experimental results, we compare with numerical simulations. For the large atom numbers used in this work, exact diagonalization methods are too expensive; therefore, we employ MPS methods as described in this section.

Method. MPS methods are well documented in the literature^{49,50}, so we focus here on the aspects important for the discussion in this paper.

MPS methods approximate the physical state by a linear network of N tensors, one at each site. Initially developed for one-dimensional many-body systems, the method is also successful on two-dimensional systems of limited width⁵¹. In our case, the $L \times L$ square lattice is mapped row by row to a linear tensor network; for the triangular arrays, the mapping is similar except that the rows have variable width. The MPS approximation is controlled by the bond dimension χ , which limits the maximum amount of entanglement between consecutive subsystems. An MPS with bond dimension χ can exhibit at most an entanglement entropy of $S=\ln(\chi)$ for a bipartition into two connected chains.

For ground-state wavefunctions of gapped, local Hamiltonians, one expects the entanglement entropy of subsystems to follow an area law⁵². This means that the entanglement entropy between two

subsystems is proportional to the length (or area) of the perimeter of the subsystems, and not proportional to their volume. When considering a time-dependent situation as we do here, the entanglement structure can become more complicated, and, for example, change to a volume law if long times after a quench are studied. As we typically fix the duration of our sweeps while scaling up the system size, we are effectively still dealing with an area-law situation. Applying these considerations to the square and the triangular lattice arrays, we are simulating systems with a maximal entanglement entropy between subsystems proportional to the width of the clusters, that is, $S \approx L$ for the square arrays. This translates into a scaling of the required bond dimension $\chi \approx \exp(\alpha L)$ for simulations of constant accuracy. On the basis of this scaling, we are able to reach widths of $L=10$ for the square lattice and a similar width for the triangular array ($N=108$) with a bond dimension of up to $\chi=512$ (see discussion below).

For the unitary time evolution, we use the time-dependent variation principle^{53,54}, which works by projecting the Hamiltonian onto the state's tangent space and then applying the time evolution operator for a small time step. At each step, we can use either a single-site or a two-site algorithm. Both algorithms give equally precise results depending on the chosen bond dimension. The single-site algorithm is much faster than the two-site algorithm, but, in contrast, does not allow for a growth of the MPS' bond dimension. The simulation starts in the initial product state, which evolves in time according to the Hamiltonian equation (1), at first using the two-site variant until the bond dimension is saturated to a certain chosen value χ , and then we switch to the single-site variant to increase the performance. For the largest systems ($N \approx 100, \chi=512$), this switch of the algorithm typically happens at around one-third of the time evolution and gives a speed up of a factor two to three per time step.

For every system size, these simulations are repeated for 30 to 70 different realizations of random lattice positions, and include other experimental uncertainties, described in the 'Effect of imperfections on larger arrays' section. We use the implementation of time-dependent variation principle provided by the python package TeNPy⁵⁵. The computationally most expensive simulations for the 10×10 square with a bond dimension of $\chi=512$ take up to 14 days for a single disorder instance. We use computer clusters to simultaneously simulate around 50 disorder instances.

Sampling of MPS wavefunctions. The experiment delivers snapshots of the state of the system projected to the Rydberg Fock space. From this data, one can determine local densities, density correlation functions and sublattice histograms. These quantities can also be obtained from exact diagonalization, as well as the classical and quantum Monte Carlo algorithms. With the MPS method, local densities and correlations can also be obtained easily by tensor contractions. However, the sampling of the Fock space snapshots is not so simple. Although the weight of a given configuration can be efficiently obtained by contracting the MPS network with the snapshot configuration as the input on the physical legs, it is less straightforward to find the most probable configurations out of the 2^N possible states.

We devised an algorithm to generate statistically independent snapshots of a given MPS wave function. (1) Pick an arbitrary site i among the n unprojected sites of the normalized MPS, and determine the diagonal elements of the single-site reduced density matrix $p_g^{(i)}$ and $p_e^{(i)}$ (for the ground state ($|\downarrow\rangle$) and excited state ($|\uparrow\rangle$), respectively), which sum up to one. (2) Draw a random number $r \in [0, 1]$ and select the ground state if $r < p_g^{(i)}$ or else select the excited state. Apply the single-site projector for the selected subspace, effectively fixing the physical leg of that site's tensor. (3) The remaining MPS with $n-1$ unprojected sites is normalized to the value of $p_{\text{gl}e}^{(i)}$, depending on the randomly selected subspace in the previous step. Thus, we divide the MPS by that value to normalize it to 1. (4) Repeat the process until there are no unprojected sites remaining.

It does not matter whether the sites to be projected are picked randomly or in sequence; however, the latter provides the opportunity to optimize the generation of thousands of snapshots by pre-contracting the tensor network. We usually generate 1,000 to 10,000 snapshots for each data point shown. The algorithm presented here is related to the ‘collapse’ step in ‘minimally entangled typical thermal state’ MPS algorithms for finite temperature simulations⁵⁶.

In Extended Data Fig. 1a, b, we compare the average Rydberg density $n = \sum_i \langle n_i \rangle / N$ and the correlator $C_{0,1}$ during the time evolution on a 10×10 square lattice computed by standard tensor contractions (black curves) to their value from a sample average of 1,000 snapshots, generated with the algorithm discussed above (blue dots). The perfect agreement demonstrates that the devised algorithm successfully samples the MPS wave function.

Bond dimension χ dependence. Owing to the aforementioned scaling of the computational complexity of the problem with χ , a trade-off between accuracy and available computational resources has to be achieved. In Extended Data Fig. 1c–f, we analyse the scaling of relevant observables used in this paper with the bond dimension χ , including experimental imperfections. Both the average Rydberg density n (Extended Data Fig. 1c) and the order parameter m_{stag} (Extended Data Fig. 1d) show only a weak dependence on χ for small times t_{off} . As expected, for larger times, the variation with χ becomes stronger, in particular for m_{stag} . Nevertheless, this variation remains small even at the end of the sweep and, notably, the uncertainty from different interaction disorder instances, shown by the shaded regions, is comparable to the variation between the lowest and largest bond dimensions.

In Extended Data Fig. 1e, f, we plot n and m_{stag} at the end of the sweep versus $1/\chi$ for different system sizes. For $L = 6$, simulations with up to $\chi = 512$ reveal a nice convergence for these observables, and the larger systems show only a slight dependence on χ . The variation resulting from χ is again smaller than that of the random U_{ij} , illustrated by the lighter lines.

To summarize, our MPS simulations for systems up to $L = 10$ are reliable to characterize and benchmark the experimental results, although they might not be fully converged in χ with regard to other observables, such as the entanglement entropy. Finally, we want to mention that reliable simulations of the dynamics for the largest experimental results achieved in this paper ($L = 14$) seem to be out of reach with currently available computational hardware, because of the exponential scaling of χ with linear system size L .

Benchmarking the platform

In this section, we discuss experimental imperfections, and systematically compare the results of the experiment with numerical simulations. We first investigate the coherence of the laser excitation for a single atom, and then introduce the imperfections relevant to the many-atom case.

Coherence of single-atom laser excitation. To investigate the efficiency and the coherence of the Rydberg excitation on a single atom, we drive Rabi oscillations between the $|\downarrow\rangle$ and $|\uparrow\rangle$ states. The results are shown in Extended Data Fig. 2a, where the oscillations are fitted by a damped sine $Ae^{-\Gamma t} \cos(\Omega t) + B$, with A and B being the amplitude and the offset of the oscillation, respectively. We obtain a decay rate $\Gamma = 0.04(1) \mu\text{s}^{-1}$ owing to spontaneous emission from the intermediate state and to the shot-to-shot fluctuations of the laser power (about 1%). In Extended Data Fig. 2b, we show a magnification of the first period, from which we measure a 97.3(8)% probability of transferring a single atom to the $|\uparrow\rangle$ state with a π -pulse. For this experiment, following the methods outlined in ref.⁴⁸, we measure $\varepsilon = 0.4(2)\%$ and infer from simulation using the experimental parameters $\varepsilon' = 1.9(1)\%$. When accounting for these detection errors, we extract a probability of 99.1(8)% to transfer a single atom to the $|\uparrow\rangle$ state.

Benchmarking the 4×4 array. Here we investigate the dynamics of the system for different sweeps on the 4×4 array. This system size can be fully simulated by solving the Schrödinger equation, for which we include the detection errors (here $\varepsilon = 1\%$ and $\varepsilon' = 3\%$). We assess the adiabaticity of the drive by performing three sweeps of durations 2.5 μs , 4 μs and 8 μs . The parameters of the sweeps, shown in Extended Data Fig. 3a, are as follows: at a detuning $\delta/2\pi = -8$ MHz, Ω is linearly increased from 0 to about $2\pi \times 1.4$ MHz, we then linearly sweep the detuning to about 2 MHz while keeping Ω constant, and finally decrease Ω to 0. As we drive a two-photon transition, the atoms experience a changing light shift as Ω is swept. We counteract this effect by changing δ accordingly. We use as observables the average Rydberg density n and staggered magnetization, m_{stag} . For all sweeps, we observe a good agreement between experiment and simulation, especially in the evolution of n . As expected, short sweeps lead to oscillations in the evolution of n due to a failure to adiabatically drive the system. This is confirmed by the value of m_{stag} at the end of the sweep, about 0.5, which would be 1 if the sweep were adiabatic. As the sweep time increases, this oscillatory behaviour is reduced and the value of m_{stag} increases.

To understand the discrepancies between the Schrödinger equation results and the data, we consider the potential experimental imperfections relevant for many-atom systems. The first is the disorder in atomic positions, which comes from two effects: (1) the static disorder in the trap positions (standard deviation of about 100 nm), and (2) the finite temperature (10 μK) of the atoms leading to shot-to-shot fluctuations in atom position with a standard deviation of $\sigma_r = 170$ nm in the plane of the array and $\sigma_z = 1 \mu\text{m}$ in the transverse direction. This results in a spatially correlated, non-Gaussian distribution of the interaction energy U_{ij} (see also Extended Data Fig. 4e, f)⁵⁷. This effect is included in simulations by repetitions with randomly assigned atom positions chosen from a Gaussian distribution with the mentioned standard deviations. We run simulations of the dynamics and average over many runs of the distribution in interaction energies. The runs are shown in Extended Data Fig. 3b, c in light grey, with the average Schrödinger equation $\langle U_{ij} \rangle$ in black. This disorder has very little influence on the results and cannot explain the remaining disagreement. Another potential source of imperfection comes from the finite size of the 1,013-nm beam, leading to inhomogeneous Ω and δ (due to the light shift of the two-photon transition) across the array; however, on this small system, the inhomogeneity is found to have negligible effect on the results. The observation that the discrepancy is largest for the longest sweep duration indicates that decoherence has an important role.

To study this effect, we solve the master equation, for which the time evolution of the density matrix $\rho(t)$ describing the instantaneous state of all the atoms is given by

$$\frac{d}{dt}\rho = -\frac{i}{\hbar}[H, \rho] + \mathcal{L}[\rho], \quad (3)$$

with a Liouvillian

$$\mathcal{L}[\rho] = \sum_i \frac{\gamma}{2} (2n_i \rho n_i - n_i \rho - \rho n_i), \quad (4)$$

where $n_i = |\uparrow\rangle\langle\uparrow|_i$. We use a decoherence rate $\gamma = 0.05 \mu\text{s}^{-1}$, which describes well the single-atom Rabi oscillation shown in Extended Data Fig. 2a, when accounting for the shot-to-shot fluctuations of the laser power. These numerical results, shown by red dashed lines in Extended Data Fig. 3b, c, agree closely with the experimental data, indicating that decoherence at the single-particle level is sufficient to describe the system.

We conclude from these studies that there is an optimized sweep duration that has to be (1) long enough to cross the gaps as adiabatically as possible and (2) short enough to avoid strong decoherence effects.

Throughout this paper, we limit the duration of the sweeps to be about 6–7.5 μs to fulfil these two conditions.

Effect of imperfections on larger arrays. For larger arrays, we use the MPS method, described in detail in the ‘Matrix product states’ section to calculate the dynamics of the systems during the sweeps.

We first perform the programmed simulation, without experimental imperfections, for the 6×6 array, the 8×8 array and the 10×10 array, using the same sweep for each array. Extended Data Fig. 4g shows the evolution of n and m_{stag} , with the experimental data as purple points and the blue line showing the MPS results. We find good agreement over the first 1.5 μs , after which we observe an overshoot in the experimental results in both n and m_{stag} for all system sizes. We also observe that m_{stag} eventually saturates on the experiment at lower values than the MPS, and that this effect worsens for larger systems.

We therefore include in the MPS the imperfections discussed in the previous section, and illustrated in Extended Data Fig. 4a–f for the 10×10 array, starting from the experimentally measured sweep shape, adding the inhomogeneous fields δ_i and Ω_i , the detection deficiency and, finally, the shot-to-shot fluctuations of the interaction energies caused by the fluctuating atom positions. The results are shown in Extended Data Fig. 4g. The imperfections have very little effect on n , and are not able to explain the overshoot, in n and m_{stag} , at intermediate times. However, at later times, we observe better agreement for all system sizes. For the 6×6 array and the 8×8 array, each imperfection has a small contribution, which tends to decrease the final value of m_{stag} . For the 10×10 array, the largest contribution to the disagreement with the MPS real sweep result is the inhomogeneity of the fields. This is unsurprising as the waist of the 1,013-nm laser is comparable to the size of the array.

A final imperfection we consider is the loss of atoms during the rearrangement process, leading to a probability that the prepared array is not perfect. After the rearrangement, we take an image of the atoms to check the number of vacancies (missing atoms) in the target structure. In Extended Data Fig. 5a, we show the histogram of the number of vacancies for the 14×14 array, for which around 17,000 experiments have been conducted, with an average filling fraction of about 98%. Owing to our high experimental repetition rate of 1–2 Hz, we can post-select the experiments for which the rearrangement process was successful. We do this for all results presented in the main text. To check the effect of vacancies on the preparation of the AF order, we measure m_{stag} as a function of the filling fraction. To decrease the filling fraction, we increase the number of allowed vacancies. The results are shown in Extended Data Fig. 5b. We observe a substantial difference in m_{stag} , between approximately 99%-filled arrays and defect-free arrays, of approximately 10%. This highlights the importance of considering only perfect arrays.

Long-term stability. We now discuss the long-term stability of the experimental setup. We do this analysis on the 8×8 array by recording the value of the staggered magnetization m_{stag} at different times t_{off} during the sweep shown in Fig. 2a. The results are presented in Extended Data Fig. 6. Each point represents a measurement, with approximately 300 snapshots recorded over approximately 20 min, giving a standard error on the mean that is smaller than the marker size. We repeat the full curve several times over a duration of about 15 h and observe a spread of m_{stag} throughout the sweep. This is due to long-term instabilities of the experimental setup. These are mainly drifts in the beam pointing and power of the Rydberg excitation lasers, which slightly change the path of the sweep in the phase diagram, thus affecting the quality of the prepared AF order. The dashed line is a phenomenological fit to the data and is indicative of the mean evolution of m_{stag} regarding the long-term drifts of the setup. We use the standard deviation on the fit for the error bars shown on the final points in Fig. 2c, d and Fig. 4b.

Growth of AF order. To further compare the MPS calculations to the experimental results, we use the snapshot technique, described in the ‘Sampling of MPS wavefunctions’ section, to plot the connected correlation maps and the m_{stag} histograms for each time step in the sweep on the 10×10 array. These are shown in Extended Data Fig. 7. The $C_{k,l}$ maps show that the correlations are beginning to develop between 1.3 μs and 1.7 μs , and are growing from nearest neighbour across the array. By 3.8 μs , the expected correlation pattern is filling the entire array, and from then on, the strength of the correlations continues to increase. The corresponding m_{stag} histograms show the growth in the number of Rydberg excitations as the distribution of points moves from about (0, 0) to higher values of $n_A + n_B$. As the correlations begin to grow across the array, we can see the distribution of points stretching along the diagonal, and, after 3.8 μs , points start to conglomerate around the corners ($N/2, 0$) and $(0, N/2)$. The MPS results show qualitative agreement throughout the sweep for both observables, with slight differences appearing at times that correspond to disagreements in Extended Data Fig. 4g. This verifies that the dynamical evolution of the atomic system is well approximated by the MPS calculations, including known uncertainties, for all observables. This confirms that we understand and have good control over our platform.

Quantum real-time evolution versus classical equilibrium

In this section, we give details on the comparison between the quantum real-time evolution and a classical equilibrium description. We also show that the real-time evolution from MPS simulations does not thermalize and cannot be described by a classical equilibrium distribution, similar to the results for the experiment presented in the main text.

Extracting a classical temperature. For a comparison with the classical Hamiltonian ($\Omega = 0$)

$$H_{\text{class}}[\delta] = \sum_{i < j} U_{ij} n_i n_j - \sum_i \hbar \delta_i n_i, \quad (5)$$

with $n_i \in \{0, 1\}$, we perform Metropolis Monte Carlo simulations with single-spin-flip updates. The results are averaged over 500 individually equilibrated samples of random atom positions. We take interactions up to a Euclidean distance of $5.2a$, or couplings $U_{ij} \geq 9.9 \times 10^{-5}$ MHz into account. Note that interactions up to a Euclidean distance of $3.3a$, or $U_{ij} \geq 1.5 \times 10^{-3}$ MHz produce nearly identical behaviour on the scales considered here. The δ_i are chosen to reflect the experimental setup, shown in Extended Data Fig. 4d.

To assign a hypothetical temperature T_{hyp} to the dynamical state of the quantum system, we compute the classical energy for the instantaneous state $|\Psi(t_{\text{off}})\rangle$,

$$E_{\text{class}}(t_{\text{off}}) = \langle \Psi(t_{\text{off}}) | H_{\text{class}}[\delta(t_{\text{off}})] | \Psi(t_{\text{off}}) \rangle \quad (6)$$

from the corresponding classical Hamiltonian in equation (5). As we do not measure the atom positions for each individual experimental snapshot, we assign the interactions $U_{ij} = U_{\text{nnb}} / (r_{ij}/a)^6$ to compute E_{class} , where U_{nnb} is the atom-position disorder averaged nearest-neighbour interaction (Extended Data Fig. 4f). Using classical Monte Carlo, we then estimate the classical thermodynamic partition function and compute the energy expectation value for the same classical Hamiltonian for a temperature T

$$E_{\text{class}}^{\text{MC}}(T) = \sum_c H_{\text{class}}(c) e^{-\beta H_{\text{class}}(c)} / Z, \quad (7)$$

where we sum over all classical spin configurations c and have defined $\beta = 1/(k_B T)$, where k_B is the Boltzmann constant, and $Z = \sum_c e^{-\beta H_{\text{class}}(c)}$.

Article

The hypothetical temperature $T_{\text{hyp}}(t_{\text{off}})$ during the sweep is then computed by matching

$$E_{\text{class}}(t_{\text{off}}) \equiv E_{\text{class}}^{\text{MC}}(T_{\text{hyp}}(t_{\text{off}})), \quad (8)$$

as illustrated in Extended Data Fig. 8a.

In Extended Data Fig. 8d, we show T_{hyp} during the experimental state preparation process for different system sizes. At $t = 0$, the system is in the ground state of H_{class} with $T_{\text{hyp}} = 0$, as we consider only arrays without any vacancies, and all atoms are in their ground state. During the first parts of the protocol where Ω is turned on and δ is increased to its final value, the hypothetical temperature strongly increases. This increase is mainly related to H_{class} not fully describing the quantum driving Hamiltonian H_{Ryd} .

During the ramp-down process ($t_{\text{off}} > 1.5 \mu\text{s}$, $\delta = \delta_f$) the boundary to the AF phase is crossed, and we observe a strong ‘cooling’ of the system. At the end of the sweep, we reach very low hypothetical temperatures close to or even below the infinite system size critical temperature T_c (see the following section). The finite temperature at the end of the sweep reflects that the state preparation is not perfectly adiabatic with the durations possible in the experiment.

Classical critical temperature. To provide a natural scale for T_{hyp} , we compute the critical temperature for the Hamiltonian parameters at the end of the considered sweep ($\Omega = 0$), which is defined as the temperature below which the classical system is ordered in the thermodynamic limit. The critical temperature $T_c/U = 0.298(1)$ is extracted from the finite-size extrapolation of the Binder cumulant $U_2 = \frac{3}{2}(1 - \langle m_{\text{stag}}^4 \rangle / 3 \langle m_{\text{stag}}^2 \rangle^2)$ crossing points as presented in Extended Data Fig. 8b⁵⁸. Simulations to obtain the Binder cumulant have been performed for systems with homogeneous $\hbar\delta/U = 1.075$ (corresponding to $\delta_f = 2\pi \times 2 \text{ MHz}$), again using 500 samples of random atom positions with an average nearest-neighbour interaction $U/h = U_{\text{nnb}}/h = 2\pi \times 1.86 \text{ MHz}$, an Euclidean interaction range of $5.2a$ and periodic boundaries. Note that the scale T_c , which is only well defined in the infinite-size system, is provided as a reference, but does not preclude the emergence of long-range order in finite size systems as observed.

Experiment versus classical equilibrium during the sweep. In Extended Data Fig. 9a (left), we analyse the experimental cluster size distribution shortly after entering the AF region. Even at this intermediate time, we observe the presence of AF ordering in the experiment, as the distribution is centred around large values of s_{max} . During the remaining part of the time evolution in the AF region, the distribution weight further moves towards larger s_{max} until it reaches the strongly peaked distribution shown in Fig. 3c (and reproduced in Extended Data Fig. 9a, right) at the end of the sweep. Also, here the corresponding classical equilibrium distribution with a hypothetical temperature T_{hyp} is very different from the experimental one, and centred around smaller values of s_{max} .

MPS time evolution versus classical equilibrium. We show in Fig. 3 that the distribution of AF domain sizes at the end of the time evolution is strikingly different from a classical equilibrium distribution with an assigned hypothetical temperature T_{hyp} . Here we show further results for an intermediate time and at the end of the time evolution from the programmed and real MPS simulations, including experimental imperfections (Extended Data Fig. 9b, c). Again, we compare those to corresponding classical equilibrium distributions from Monte Carlo simulations. Shortly after entering the AF dome (left panels), we observe a behaviour similar to the experiment (Extended Data Fig. 9a) for both setups, where the distribution of the MPS simulations is generally shifted towards larger cluster sizes s_{max} compared with the classical distribution. At the end of the sweep (right panels), we still observe

that the simulations are not thermalized, as the MPS distributions are not matched by the classical equilibrium ones. Also, the probability of creating Néel states is enhanced compared with the classical distribution for both MPS simulations. In the programmed case, this effect is particularly strong, indicating that with experimental improvements we will gain in ground state preparation fidelity.

In Extended Data Fig. 8e, f, we show the evolution of T_{hyp} for the MPS simulations during the final part of the state preparation protocol for systems with up to 10×10 atoms for both protocols (programmed and real). Similar to the experiment, we observe a strong cooling of the system. At the end of the sweep, we observe that the extracted temperatures from the MPS simulations are somewhat lower than the ones from the experiment, for both the programmed and real cases, pointing to possible further imperfections not yet taken into account.

To conclude, one might wonder why the high probability of finding Néel states in the right panel of Extended Data Fig. 9b does not translate into a substantially lower hypothetical temperature T_{hyp} in Extended Data Fig. 8e. The main reason is the temperature dependence of the specific heat of the equilibrium system. In the gapped AF phase, the specific heat is exponentially suppressed at low temperature $C(T) \approx \exp(-U/k_B T)$ (ref. ⁵⁹). On the other hand, the excess energy $\Delta E \equiv E_{\text{class}} - E_{\text{class}}^{\text{GS}}$, with GS denoting the ground state of the system, is related to the integral of $C(T)$:

$$\Delta E = \int_0^T C(T') dT'.$$

Combining the two formulas, we infer that $T \approx 1/\log(1/\Delta E)$, that is, the matching temperature tends to zero only logarithmically slowly with ΔE going to zero.

Triangular geometries

In this section, we consider the peculiarity of the finite-sized triangular array, leading to the observed reduction in the m_{stag} histogram observed for the 2/3 phase. We also compare classical equilibrium calculations to experimental results on the triangular lattice.

Triangular 2/3 plateau. The edge of the finite-sized clusters can have an impact on the achievable ground states, which might differ from the ones expected from the corresponding bulk phase diagram. In particular, the edge sites have fewer direct neighbours than the bulk sites and, hence, they can be excited to Rydberg states at lower δ/U . For the results in this paper, this effect is particularly important for the 2/3 phase on the triangular clusters, as we will now discuss.

In Extended Data Fig. 10a, b, we show Monte Carlo results for a fixed $\hbar\delta/U = 4$ in the 2/3-filling regime at low temperature $T/U = 0.1$. It is clearly visible in the Rydberg density, n_r , that the edge sites become completely filled with Rydberg states in the ground state $T \rightarrow 0$. In particular, the Rydberg density on the edge, n_{edge} , approaches one when the temperature is reduced (Extended Data Fig. 10a, inset). Therefore, only the atoms in the bulk can take part in the formation of the 2/3-filled states, and the maximal order parameter is reduced. This can be directly observed in the sublattice magnetization histogram (Extended Data Fig. 10b), which shows that the position of the three peaks defining the 2/3 phase do not reach their maximal possible value at the edge of the outer hexagon. Instead, they are bounded by the dashed hexagon, which shows the maximum extent of the histogram for the bulk system.

The reduction of the maximum radius is rather large, as it scales with the number of sites on the boundary. In particular, for the 108-site cluster shown here, the boundary consists of 33 sites, leading to an approximately 30% reduction of the maximum radius in the histogram. This effect is not observed in the 1/3 regime as δ_f is small enough that the boundary sites also obey the AF ordering.

Time evolution versus classical equilibrium on the triangular lattice. Here we demonstrate that on the triangular lattice, the experimental state preparation protocol, again, cannot be reproduced by a classical equilibrium distribution. In Extended Data Fig. 10c, d, we show the experimentally obtained distribution of the order parameter, m_{stag} , at the end of the sweep preparing the 1/3 and 2/3 phases for the 108-atom array, and compare them to the corresponding classical distribution with hypothetical classical temperature T_{hyp} , assigned as described in the ‘Extracting a classical temperature’ section. The experimental distribution is centred at substantially larger values of m_{stag} , demonstrating an increased probability of finding highly ordered states compared with a corresponding classical annealing. In Extended Data Fig. 10e, we show, as a comparison, the distribution of m_{stag} for a 10×10 square lattice at the end of the sweep preparing the AF phase, which shows similar, but enhanced, features.

Data availability

The data presented in the figures and that support the other findings of this study are available from the corresponding author on reasonable request.

Code availability

The codes are available upon reasonable request from the corresponding author.

47. Barredo, D., Lienhard, V., de Léséleuc, S., Lahaye, T. & Browaeys, A. Synthetic three-dimensional atomic structures assembled atom by atom. *Nature* **561**, 79–82 (2018).
48. de Léséleuc, S., Barredo, D., Lienhard, V., Browaeys, A. & Lahaye, T. Analysis of imperfections in the coherent optical excitation of single atoms to Rydberg states. *Phys. Rev. A* **97**, 053803 (2018).
49. Schollwöck, U. The density-matrix renormalization group in the age of matrix product states. *Ann. Phys.* **326**, 96–192 (2011).

50. Paeckel, S. et al. Time-evolution methods for matrix-product states. *Ann. Phys.* **50**, 167998 (2019).
51. Stoudenmire, E. M. & White, S. R. Studying two-dimensional systems with the density matrix renormalization group. *Annu. Rev. Condens. Matter Phys.* **3**, 111–128 (2012).
52. Eisert, J., Cramer, M. & Plenio, M. B. Area laws for the entanglement entropy. *Rev. Mod. Phys.* **82**, 277–306 (2010).
53. Haegeman, J. et al. Time-dependent variational principle for quantum lattices. *Phys. Rev. Lett.* **107**, 070601 (2011).
54. Haegeman, J., Lubich, C., Oseledets, I., Vandereycken, B. & Verstraete, F. Unifying time evolution and optimization with matrix product states. *Phys. Rev. B* **94**, 165116 (2016).
55. Hauschild, J. & Pollmann, F. Efficient numerical simulations with Tensor Networks: Tensor Network Python (TeNPy). *SciPost Phys. Lect. Notes* **5** <https://doi.org/10.21468/SciPostPhysLectNotes.5> (2018).
56. Stoudenmire, E. M. & White, S. R. Minimally entangled typical thermal state algorithms. *New J. Phys.* **12**, 055026 (2010).
57. Marcuzzi, M. et al. Facilitation dynamics and localization phenomena in Rydberg lattice gases with position disorder. *Phys. Rev. Lett.* **118**, 063606 (2017).
58. Binder, K. Finite size scaling analysis of Ising model block distribution functions. *Z. Phys. B* **43**, 119–140 (1981).
59. Onsager, L. Crystal statistics. I. A two-dimensional model with an order–disorder transition. *Phys. Rev.* **65**, 117–149 (1944).

Acknowledgements This project has received funding from the European Union’s Horizon 2020 research and innovation programme under grant agreement number 817482 (PASQuaS). M.S. acknowledges support by the Austrian Science Fund (FWF) through grant number P 31701 (ULMAC). D.B. acknowledges support from the Ramón y Cajal programme (RYC2018-025348-I). K.-N.S. acknowledges support by the Studienstiftung des Deutschen Volkes. A.A.E. and A.M.L. acknowledge support by the Austrian Science Fund (FWF) through grant number I 4548. The computational results presented have been achieved in part using the Vienna Scientific Cluster (VSC) and the LEO HPC infrastructure of the University of Innsbruck.

Author contributions P.S., M.S., H.J.W. and A.A.E. contributed equally to this work. P.S., H.J.W., D.B., K.-N.S. and V.L. carried out the experiments. M.S., A.A.E., L.-P.H. and T.C.L. performed the simulations. All authors contributed to the data analysis, progression of the project, and on both the experimental and theoretical side. All authors contributed to the writing of the manuscript.

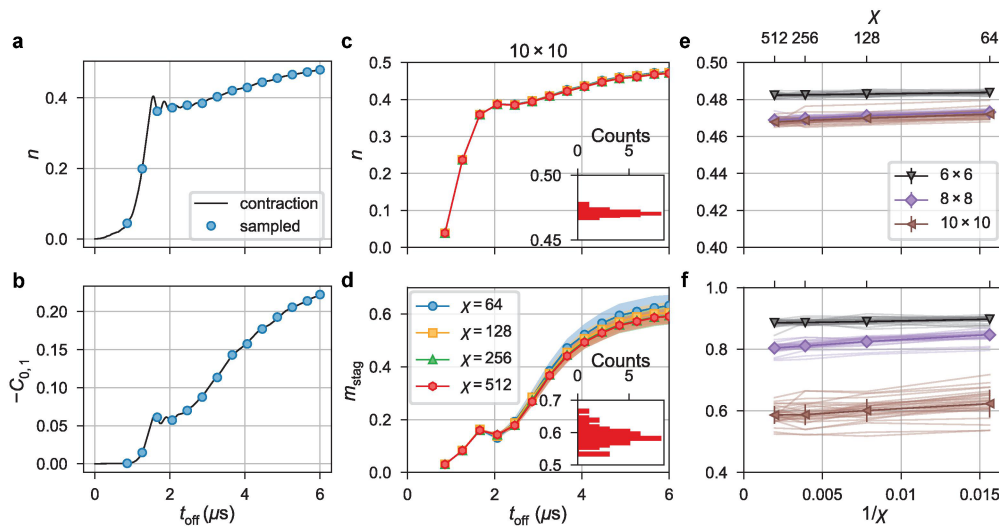
Competing interests A.B. and T.C.L. are co-founders and shareholders of Pasqal.

Additional information

Correspondence and requests for materials should be addressed to P.S.

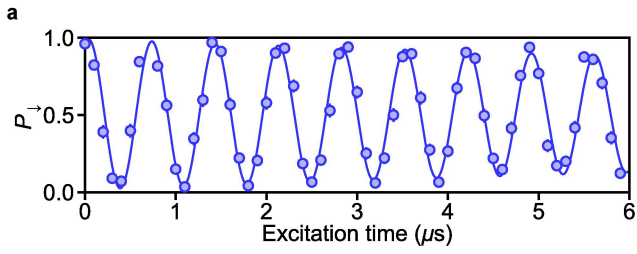
Peer review information *Nature* thanks the anonymous reviewer(s) for their contribution to the peer review of this work.

Reprints and permissions information is available at <http://www.nature.com/reprints>.

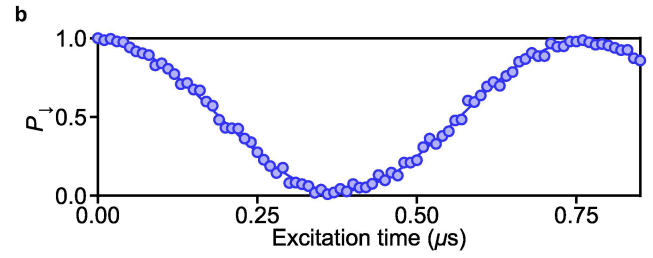


Extended Data Fig. 1 | MPS sampling and scaling with bond dimension χ . **a, b,** Average Rydberg density **(a)** and nearest-neighbour correlation function **(b)** during the MPS state dynamics on the 10×10 square lattice. The black lines show the observables computed from standard tensor contraction and the blue dots show the corresponding sample average of 1,000 generated snapshots. **c-f,** Scaling with bond dimension. **c, d,** Rydberg density **(c)** and

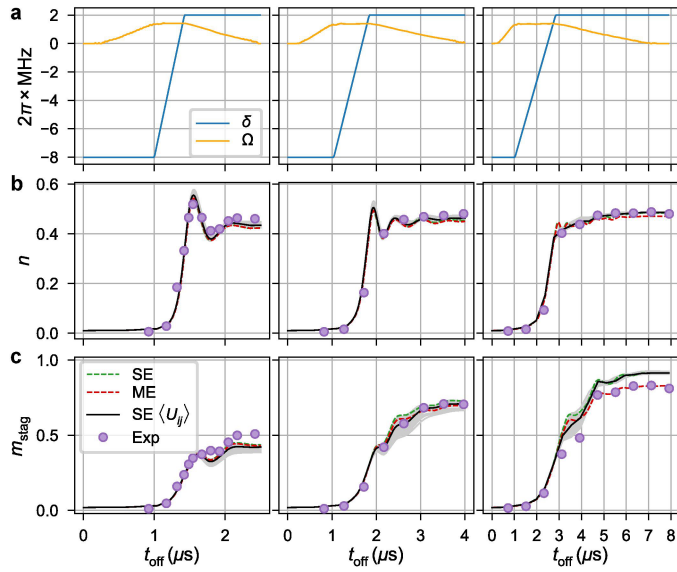
order parameter m_{stag} **(d)** during the MPS state dynamics, including experimental imperfections, for different χ on the 10×10 square lattice. The insets show the distribution due to the multiple U_{ij} disorder realizations, at final $t_{\text{off}} = 6 \mu\text{s}$ for $\chi = 256$. **e, f,** Scaling of n **(e)** and m_{stag} **(f)** with χ at the end of the state preparation protocol for different system sizes. The lightly coloured lines show the multiple disorder instances.



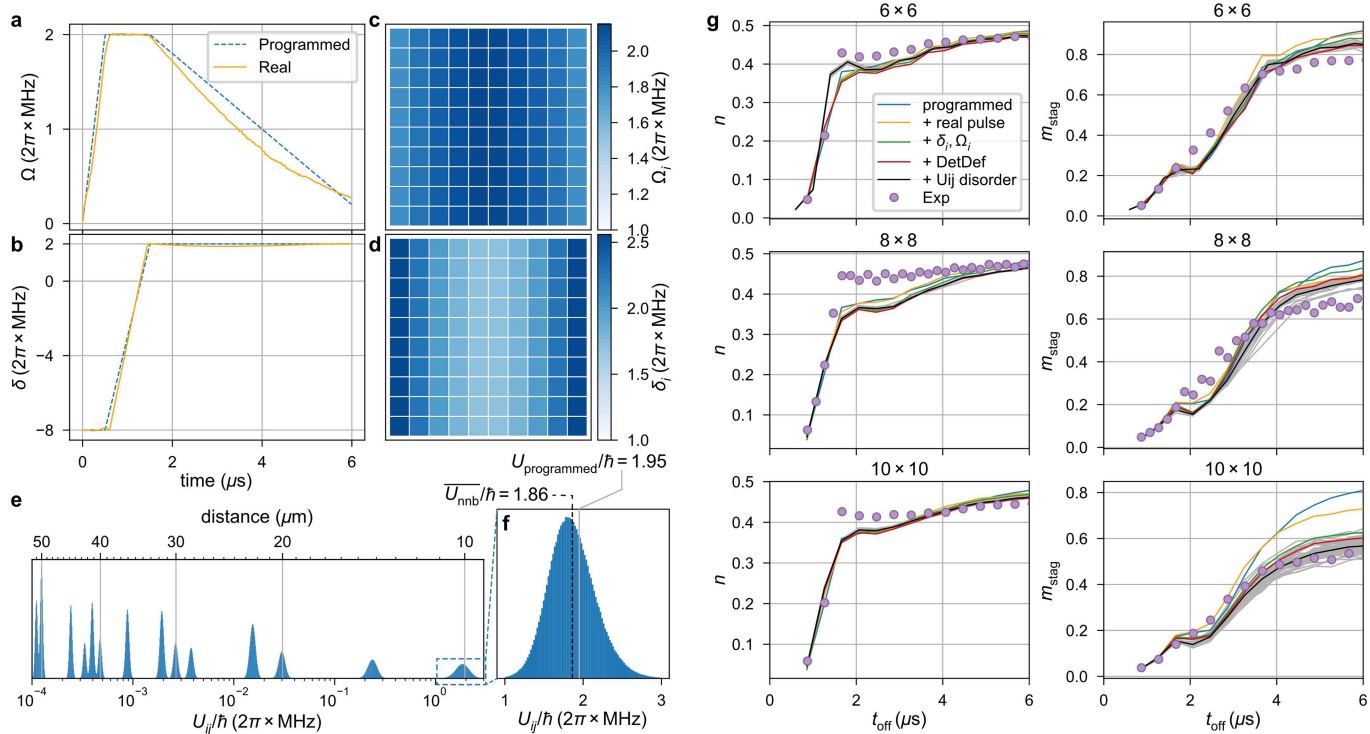
Extended Data Fig. 2 | Testing the coherence of the Rydberg excitation on a single atom. a, Rabi oscillations showing the probability of measuring the atom in $|\downarrow\rangle$ as a function of the excitation time. The line is a fit to the data by the function $Ae^{-\Gamma t}\cos(\Omega t) + B$, yielding $\Gamma = 0.04(1) \mu\text{s}^{-1}$, $\Omega = 2\pi \times 1.32(1) \text{ MHz}$,



$A = 0.488(3)$ and $B = 0.507(3)$. **b,** High-resolution measurement of the first period of the oscillation. Error bars are statistical and often smaller than marker size.



Extended Data Fig. 3 | Benchmarking multiple sweeps on the 4×4 array.
a–c, Time evolution of sweep shape (**a**), Rydberg density (**b**) and staggered magnetization (**c**) for three distinct sweeps (of durations $2.5 \mu\text{s}$ (left), $4 \mu\text{s}$ (middle) and $8 \mu\text{s}$ (right)) on the 4×4 array. In **b, c**, experimental data are shown in purple circles and the green (red) dashed lines show solutions to the Schrödinger equation (Lindblad master equation, equation (3)). The solid grey lines show solutions of the Schrödinger equation for several random instances of the interaction disorder (see text), the black line is the average over these instances.

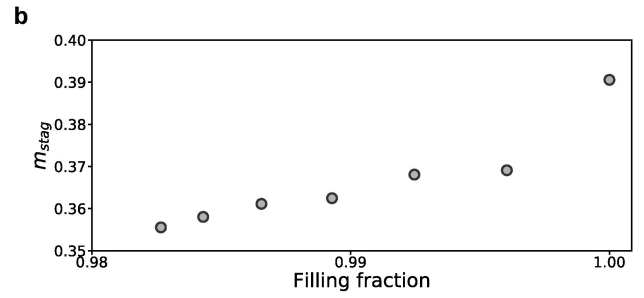


Extended Data Fig. 4 | Experimental imperfections. **a, b**, Sweep shape for the average Rabi frequency Ω (**a**) and the average detuning δ (**b**) versus time. The dashed line shows the proposed protocol and the solid line shows the experimentally obtained parameters. **c, d**, Spatial dependence of Ω (**c**) and δ (**d**) at the maximal values during the protocol. **e, f**, Distribution of the Rydberg interactions U_{ij} caused by the fluctuations in the atom positions. **e**, The long-range interactions up to a distance of about $50 \mu\text{m}$. **f**, The distribution of the nearest-neighbour interactions. The dashed vertical line shows the average nearest-neighbour interaction U_{nnb} . The vertical grey line shows, as a reference, the programmed value for non-fluctuating atoms $U_{\text{programmed}}$. **g**, The left (right)

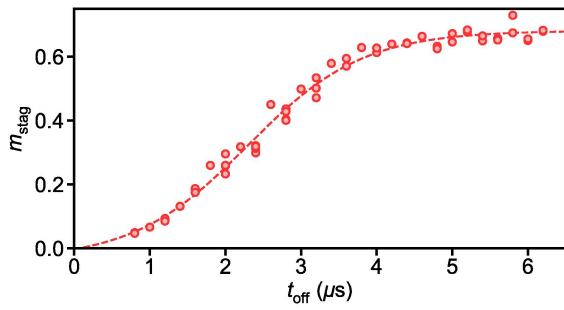
column shows the average density (order parameter m_{stag}) during the sweep for different sizes of the square lattice. Different lines show successive additions of imperfections on the MPS simulations. Starting from the programmed pulse shape without imperfections (blue), we include the real pulse shape measured in the experiment (yellow), add the inhomogeneous fields (green), apply the detection deficiency (red) and, finally, include the interaction disorder from fluctuations in the atom positions. The grey lines show individual samples of atom positions and the black line shows the sample average. Experimental data are shown by circles.



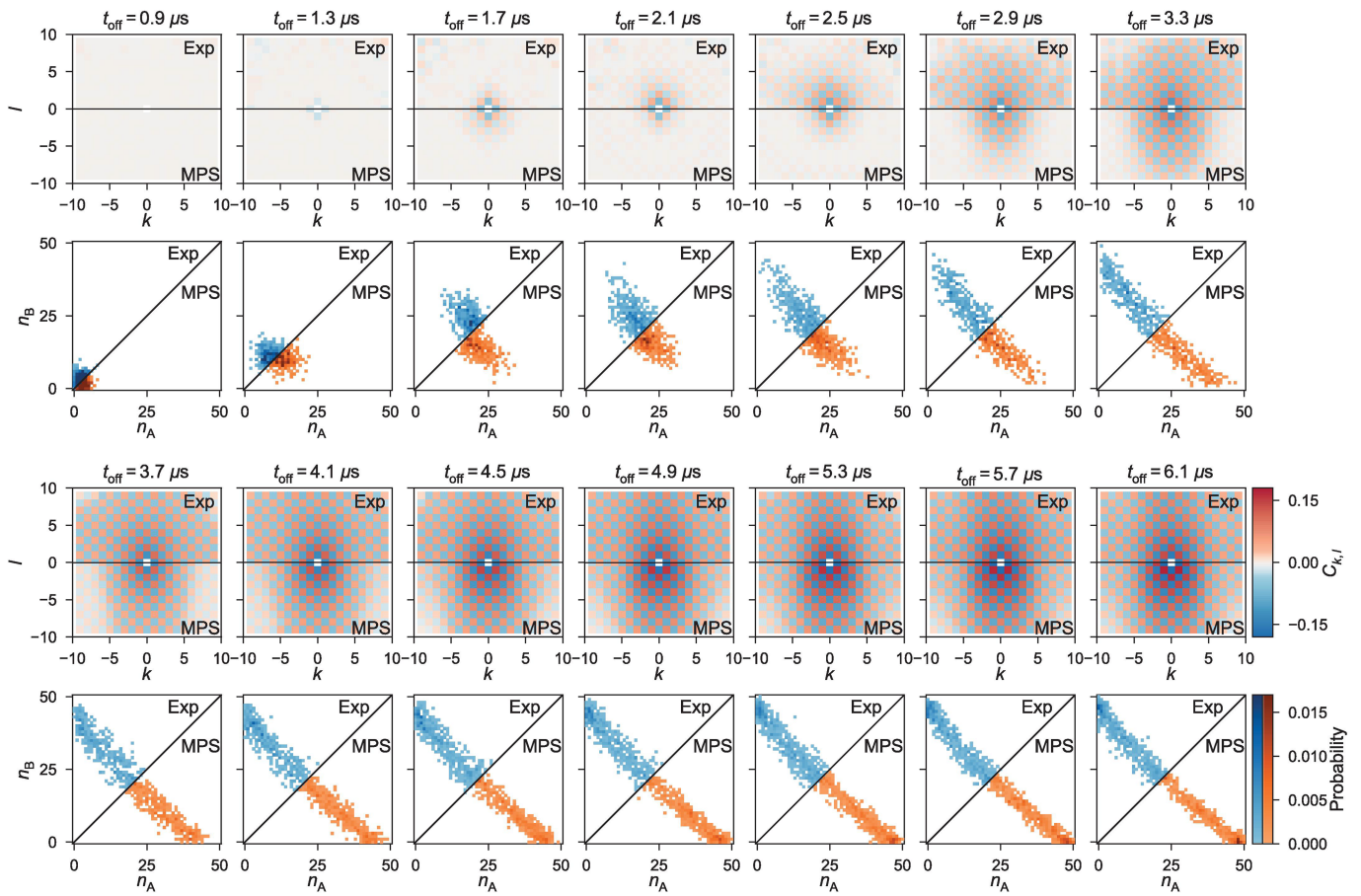
Extended Data Fig. 5 | Effect of vacancies on AF ordering. **a**, Histogram of the number of defects for the 14×14 array. Out of the roughly 17,000 experimental realizations shown here, we kept only the approximately 500 defect-free shots



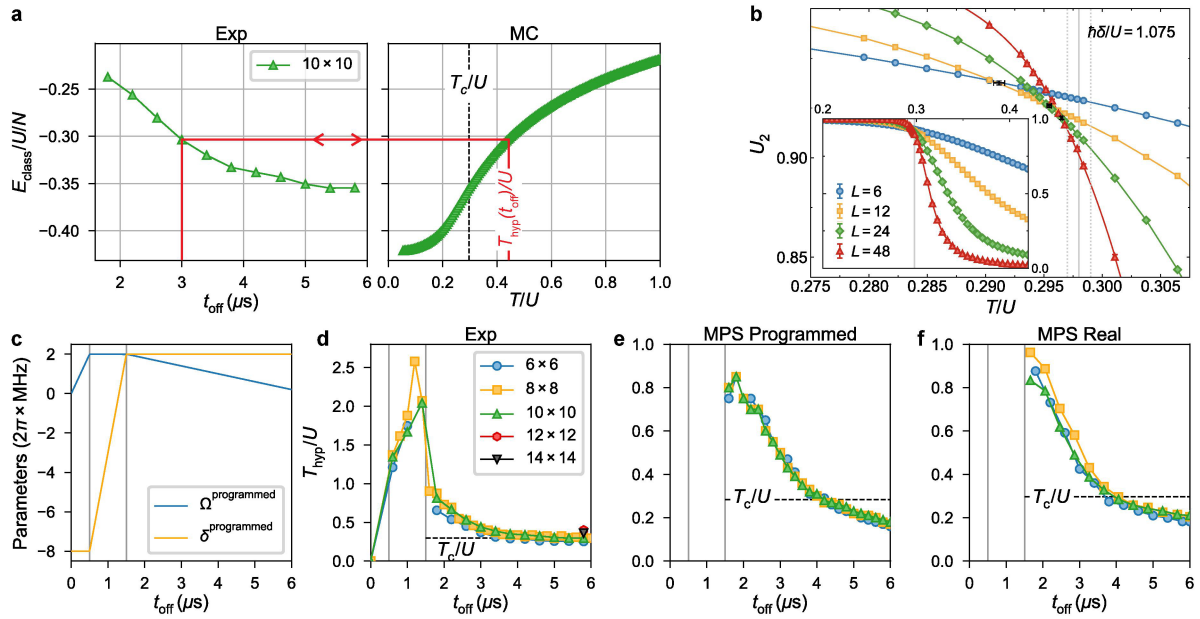
for the results presented in the main text. **b**, m_{stag} for different filling fractions. We observe a substantial increase in m_{stag} for defect-free array experiments, compared with approximately 99%-filled-array experiments.



Extended Data Fig. 6 | Long-term stability of the growth of AF ordering on the 8×8 array. Staggered magnetization m_{stag} at different times t_{off} during the sweep shown in Extended Data Fig. 2a with several measurements using the same parameters, realized over 15 h. We observe a dispersion of the measurements due to long-term drift of the experimental setup. The dashed line is a phenomenological fit to the data. The standard error on the mean is smaller than symbol size.

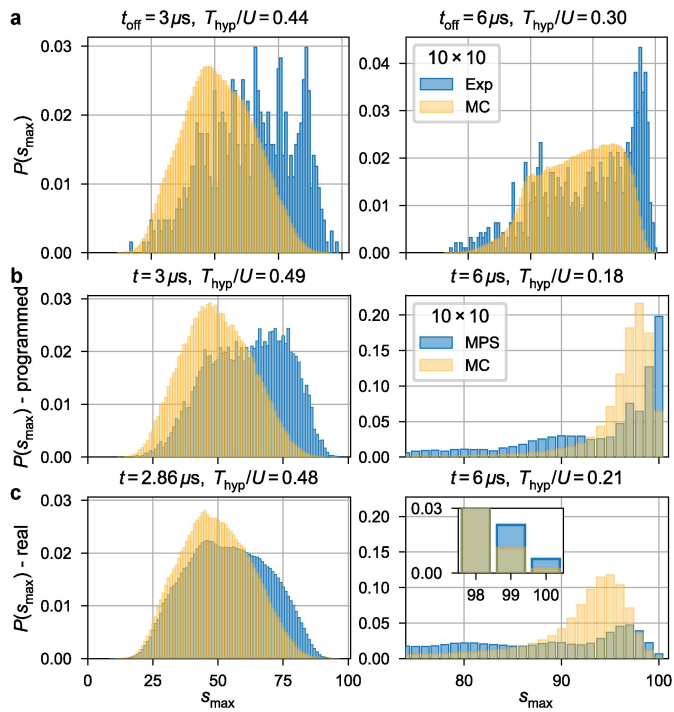


Extended Data Fig. 7 | Growth of AF ordering on a 10×10 array during the sweep. Maps of the connected correlations $C_{k,l}$ and histograms of the staggered magnetization for different times t_{off} , defined in Fig. 2. The upper (lower) part of the plots show experimental (MPS) results.

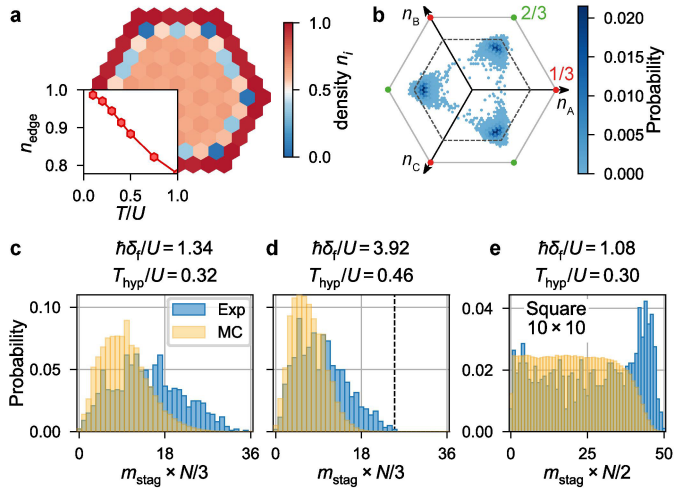


Extended Data Fig. 8 | Hypothetical temperature. **a**, Assigning a hypothetical temperature. Classical energy density for the instantaneous state $|\Psi(t_{\text{off}})\rangle$ of the experiment during the last part of the state preparation protocol (left), and for the corresponding classical equilibrium system versus temperature T (right). Here $\delta = \delta_i$ for all datasets. We assign a hypothetical temperature T_{hyp} at each time t_{off} by matching the classical energy, as illustrated by the red line. In the right panel, T_c denotes the critical temperature in the thermodynamic limit $N \rightarrow \infty$. **b**, The Binder cumulant U_2 and its $(L, 2L)$ crossing points (black markers) for different linear system dimensions L , which allow the

estimation of the critical temperature in the thermodynamic limit. The solid (dotted) grey lines indicate the finite size extrapolated T_c and its standard error. **c-f**, Evolution of the hypothetical temperature. **c**, Programmed state preparation protocol. **d-f**, Corresponding hypothetical temperatures $T_{\text{hyp}}(t_{\text{off}})$ during the sweep for different system sizes for the experiment (**d**) and MPS simulations without (**e**) and with (**f**) experimental imperfections. The dashed lines show the classical critical temperature T_c for an infinite system with disorder averaged $U/\hbar = 2\pi \times 1.86 \text{ MHz}$ for $\delta_i = 2\pi \times 2 \text{ MHz}$.



Extended Data Fig. 9 | Quantum real-time evolution versus classical equilibrium. Distribution of the largest Néel cluster sizes s_{\max} during (left) and at the end (right) of the quantum time evolution (blue) compared with the classical equilibrium results (yellow) on a 10×10 square lattice. **a**, Experimental results. **b**, MPS simulation in the setup without including any experimental imperfections. **c**, MPS simulation including the known experimental imperfections.



Extended Data Fig. 10 | Triangular geometries. **a, b,** m_{stag} histogram in the $2/3$ plateau obtained from Monte Carlo results on a 108-site triangular cluster with $\hbar\delta_f/U = 4$ and temperature $T/U = 0.1$. **a,** The real space Rydberg density n_i shows that the outermost shell becomes fully populated at low temperature, as also illustrated in the inset, which shows the Rydberg density at the edge. **b,** The corresponding sublattice magnetization histogram does not reach its full potential width (outer hexagon), as the edge sites cannot participate in the formation of the $2/3$ -filling states. The dashed hexagon shows the maximum extent of the histogram when only the sites of the system without the edge are considered. **c, d,** Quantum real-time evolution versus classical equilibrium on the triangular lattice. We plot the distribution of the triangular order parameter m_{stag} at the end of the state preparation protocols entering the $1/3$ (**c**) and $2/3$ (**d**) regimes on a 108-site triangular cluster. Blue (yellow) bars show experimental (corresponding classical) results. The dashed line in **d** shows the maximal value of m_{stag} in the $2/3$ regime induced by the cluster boundaries. **e,** Distribution of m_{stag} for a 10×10 square lattice at the end of the sweep entering the AF phase, as a comparison.